Journal of Materials Chemistry A

ROYAL SOCIETY OF CHEMISTRY

PAPER

View Article Online
View Journal | View Issue

Cite this: J. Mater. Chem. A, 2025, 13, 18900

Surface amorphized *in situ* RuO-NiFeOOH/Au islands for electrocatalytic oxygen evolution reaction†

Karthick Kannimuthu,[a] Pawan Kumar,[a] Pooja Gakhad,[b] Hadi Shaker Shiran,[a] Xiyang Wang,[c] Ali Shayesteh Zeraati,[a] Sangeetha Kumaravel,[d] Shariful Kibria Nabil,[a] Rajangam Vinodh,[a] Md Abdullah Al Bari,[agh] Maria Molina,[a] George Shimizu,[a] Yimin A. Wu,[c] Pulickel M. Ajayan,[e] Abhishek Kumar Singh,[b] Soumyabrata Roy[ef] and Md Golam Kibria *[a]

Hydrogen production *via* electrocatalytic water splitting is largely impeded by the anodic oxygen evolution reaction (OER). Herein, we report surface amorphized Ru-NiFeP/Au islands as an effective electrode for the OER in 1 M KOH, reaching a current density of 10 mA cm^{-2} at 223 mV overpotential. The *iR* corrected Tafel slope was calculated to be 32 mV dec^{-1}, while electrochemical impedance spectroscopy (EIS) studies revealed a clearly low charge transfer resistance of 0.3 Ω at 400 mV overpotential. The high electrocatalytic activity was attributed to the amorphous nature, reduced band gap, and synergism of Ru-NiFeP with Au. *In situ* surface-enhanced Raman scattering (SERS) revealed the role of FeOOH at lower overpotentials for facile OH adsorption. The evolution of NiOOH peaks at higher overpotentials for O_2 evolution coupled with synergistic Ru–O bonds to promote the OER was studied with DFT analysis. Bader charge analysis showed that the charge transfer from Fe to O is 0.17 units greater than that from Ni to O for *OH intermediate generation at the active site, and this corroborates the results from *in situ* SERS studies, where FeOOH is the active site at lower overpotentials. The bond order characteristics become more pronounced when the FeOOH/NiOOH surfaces are accessible. DFT analysis revealed a low free energy change (0.12 eV) for the rate-determining step at the RuO/NiFe-OOH surface.

Received 6th February 2025
Accepted 26th April 2025

DOI: 10.1039/d5ta00958h

rsc.li/materials-a

Introduction

The four-electron oxygen evolution reaction (OER, $4OH^- \rightarrow O_2 + 2H_2O + 4e^-$) is a key half-cell reaction involved in vital energy conversion processes, such as those occurring in water and CO_2 electrolyzers,[1] photoelectrochemical water splitting,[2] and metal–air batteries.[3] Water electrolyzers powered by renewable energy sources, such as wind and photovoltaic cells, can be utilized to produce green hydrogen.[4] However, the energy efficiency of these devices is hindered by the kinetically sluggish M–OH, M–O formation (M: metal) and subsequent O_2 evolution with $4e^-$ transfer during anodic OER. Commercial water electrolyzers require 1.8–2.0 V. Furthermore, scarce materials like IrO_2 and RuO_2 are used as OER electrodes, affecting economic viability.[5] Consequently, the search for non-noble metal electrodes with improved performance is anticipated to avoid the staggering price for the sustainable and widespread commercial utilization of alkaline water electrolyzers. In alkaline electrolytes, 3d transition metals (TMs: Fe, Co, and Ni) have been studied in detail for the OER with considerable enhancement in activity and stability.[6,7] This is related to the low crystal field activation energy with favorable M(3d)–O(2p) overlap of these TMs for facile M–OH adsorption and O_2 cleavage.[8] Recently, many reports have highlighted the use of metal oxides,[9–14] hydroxides,[15–19] and metal chalcogenides[20–23] with substantial activity. However, their applicability is limited due to low electrical conductivity. Alternatively, TM phosphides (TMPs) can deliver exceptional OER performance with superior electrical conductivity.[24–27]

[a]Department of Chemical and Petroleum Engineering, University of Calgary, 2500 University Drive, NW Calgary, Alberta, T2N 1N4, Canada
[b]Materials Research Centre, Indian Institute of Science, Bangalore 560 012, India
[c]Department of Mechanical and Mechatronics Engineering, Waterloo Institute for Nanotechnology, Materials Interface Foundry, University of Waterloo, Waterloo, Ontario N2L 3G1, Canada
[d]Department of Chemistry, Kalasalingam Academy of Research and Education, Srivilliputhur 626126, India
[e]Department of Materials Science and Nanoengineering, Rice University, 6100 Main St., Houston, TX 77030, USA
[f]Department of Sustainable Energy Engineering, Indian Institute of Technology Kanpur, Kanpur, Uttar Pradesh 208016, India. E-mail: md.kibria@ucalgary.ca
[g]Department of Mechanical Engineering, King Fahd University of Petroleum & Minerals, Dhahran, 31261, Saudi Arabia
[h]Interdisciplinary Research Center for Sustainable Energy Systems, King Fahd University of Petroleum & Minerals, Dhahran 31261, Saudi Arabia

† Electronic supplementary information (ESI) available. See DOI: https://doi.org/10.1039/d5ta00958h

TMPs act as 'pre-catalysts', and *in situ* structural studies have revealed the *operando*-generated TM oxyhydroxides (TMOOHs) as the active centers that are vital for enhancing the transport of O-intermediates.[28,29] Peng *et al.* highlighted the *in situ* oxidized Ni_2P/Fe_2P interface for the OER and elucidated the role of surface PO_4^{3-} ions and conductive bulk phosphides in accumulating charges in vacant 3p and 3d orbitals.[28] The nature of the covalent strength and inductive effect of metal phosphates was investigated by Siraj *et al.*, where the lowering of the M–O antibonding energy levels induces a positive shift of the redox potential in $Fe_3Co(PO_4)_4$ to modulate the OER activity.[30] As shown by Panlong *et al.*, the inclusion of Ru(4d) to 3d transition metals promotes O–O coupling at the Ru–O active site for OER in the Ru/NiFe LDH single atom sites.[16] Due to the M–H bond strength being similar to that of Pt and its lower costs, Ding *et al.* explored Ru-doped MnFeP/NF for efficient solar-to-hydrogen (STH) fuel generation with photo-electrocatalysis.[31] In another work, an amalgamation of Ag over Ni–Fe–P was successfully carried out by Zhiyuan *et al.*, where the non-metal P was crucial to amalgamate Ag for utilization in OER and ORR (oxygen reduction reaction) studies.[32] Understanding 'active sites' for complex OER in multi-metallic phosphides at a molecular level can bridge the gap between the catalytic structure and activity, which is crucial to develop effective catalysts.[25] Similar to phosphides, inclusion of noble metals like Ir and Ru in oxides improved the OER performance because of the surface electron distribution and oxygen vacancy sites.[33,34]

In highly active NiFe-OOH for OER, the actual active surface is always a matter of concern.[35] It was observed from *in situ* Raman studies that e_g bending (475 cm^{-1}) and A_{1g} stretching vibrations (555 cm^{-1}) confirm NiOOH as active sites.[36,37] The relative intensity (I_{475}/I_{555}) of Ni–O in NiOOH decreases in the presence of Fe, suggesting a modified local electronic environment, and it was proven that Fe promoted the $Ni(OH)_2$-to-NiOOH (active site) transformation.[36] SERS is a potent tool for the molecular detection of intermediates under an OER bias with a high spatial resolution because of its ultra-sensitivity at the low-frequency range and non-interference with water.[38] However, the sensitivity of SERS is limited to a few metals like Au and Ag. One way to overcome this limitation is a borrowing strategy, where the electrocatalyst is grown over the rough surfaces of Au.[39] This strategy helps to amplify the signals of short-lifetime species and acquires the surface properties of the electrocatalytic system. Also, the electrophilic character of Au as an 'electron sink' stabilizes the high oxidation states of the active sites during OER. Because of its O_2-repellent nature, this ensures the fast evolution of O_2 from the surface. The presence of Au assisted the conversion of oxyhydroxides. In a work by Jakob *et al.*, the Au(111) interface in cobalt oxide favored the transformation of cobalt oxyhydroxide during OER, rather than the less active bulk cobalt oxide.[40] Furthermore, in NiFe LDH systems, the use of Au as single atoms resulted in an increase in the OER activity due to the formation of NiFe oxyhydroxides.[41]

To ensure high catalytic activity, surface amorphization is another important strategy for developing 'dangling bonds' to achieve effective charge transfer due to the local short-range order.[42,43] Herein, we envisioned surface amorphization and synergism of Ru over the NiFeP/Au surface to enhance the OER activity, and explored *in situ* SERS analysis to understand the mechanisms and active sites. Initially, the Ni foam (NF) is replaced with Au *via* galvanic replacement, followed by electrodeposition to develop RuFeP/Au-Ni islands for OER in 1 M KOH. The optimized heterostructure catalyst (Ru15-NiFeP) requires an overpotential of just 223 mV to attain an OER current density of 10 mA cm^{-2}, while exhibiting a low Tafel slope (32 mV dec^{-1}). Spectroelectrochemical investigations with *in situ* SERS suggested the direct role of FeOOH surface-active sites at low overpotential and NiOOH at higher overpotential for OER. *In situ* EIS measurements in the applied potential window of 1.3–1.6 V in the OER region indicated increased O-intermediate kinetics on Ru15-NiFeP/Au compared to Au–Ni and NiFeP/Au. DFT studies confirmed that the presence of Fe induces ionic character in the Fe–O bond for the better adsorption of O-containing intermediates, while Ni (with the increased covalency) result in relatively poor O-intermediate adsorption, which is in line with *in situ* SERS outcomes. This work provides insight into the development of TMPs with improved synergy for OER, and further reveals a deeper understanding of the role of OER active sites *via in situ* SERS studies.

Results and discussion

Synthesis and characterization

Ru-NiFeP with different concentrations of Ru was developed through the electrodeposition method on a three-dimensional porous skeleton of Au–Ni formed *via* galvanic replacement, as portrayed in Fig. 1a. Notably, the entire synthesis and fabrication process was carried out at room temperature under ambient conditions and no harsh conditions were employed. The crystalline feature of Au–Ni was assessed *via* X-ray diffraction (XRD), where the peaks at 38.6° (200), 64.3° (022), and 81.4° (222) confirmed the presence of metallic Au, in addition to the metallic Ni peaks at 44.5° (111), 51.8° (200), and 76.4° (220) (Fig. S1a and b†).[44] For Ru15-NiFeP/Au, no additional characteristic peaks appeared, indicating the amorphous nature of Ru15-NiFeP. Synchrotron-based grazing incidence-wide angle X-ray scattering (GI-WAXS) analysis on Au–Ni discerned the crystalline nature of Au with sharp diffraction rings and corresponding *Q*-values (Fig. S2a and b†). Ru15-NiFeP/Au comprises similar amorphous characteristics, and is in line with the XRD results (Fig. 1b and c). Scanning electron microscopy (SEM) elemental mapping and energy dispersive X-ray spectroscopy (EDX) of Au–Ni (Fig. S3a–d†) and Ru15-NiFeP/Au (Fig. 1d) display the homogenous distribution of Ru, Fe, Ni, and P on the Au islands. For different concentrations of Ru, the formed Ru-NiFeP showed similar morphological features (Fig. S4–S6†). To gain further structural insight, high-resolution transmission electron microscopy (HR-TEM) and high-angle annular dark field-scanning transmission electron microscopy (HAADF-STEM) were employed. As shown in Fig. 1e, the HR-TEM images demonstrate the uniform sheet morphology for Au-Ni and Ru15-NiFeP over the Au-Ni layer. High-magnification TEM images of Ru15-NiFeP/Au in the nanosheets regions displayed

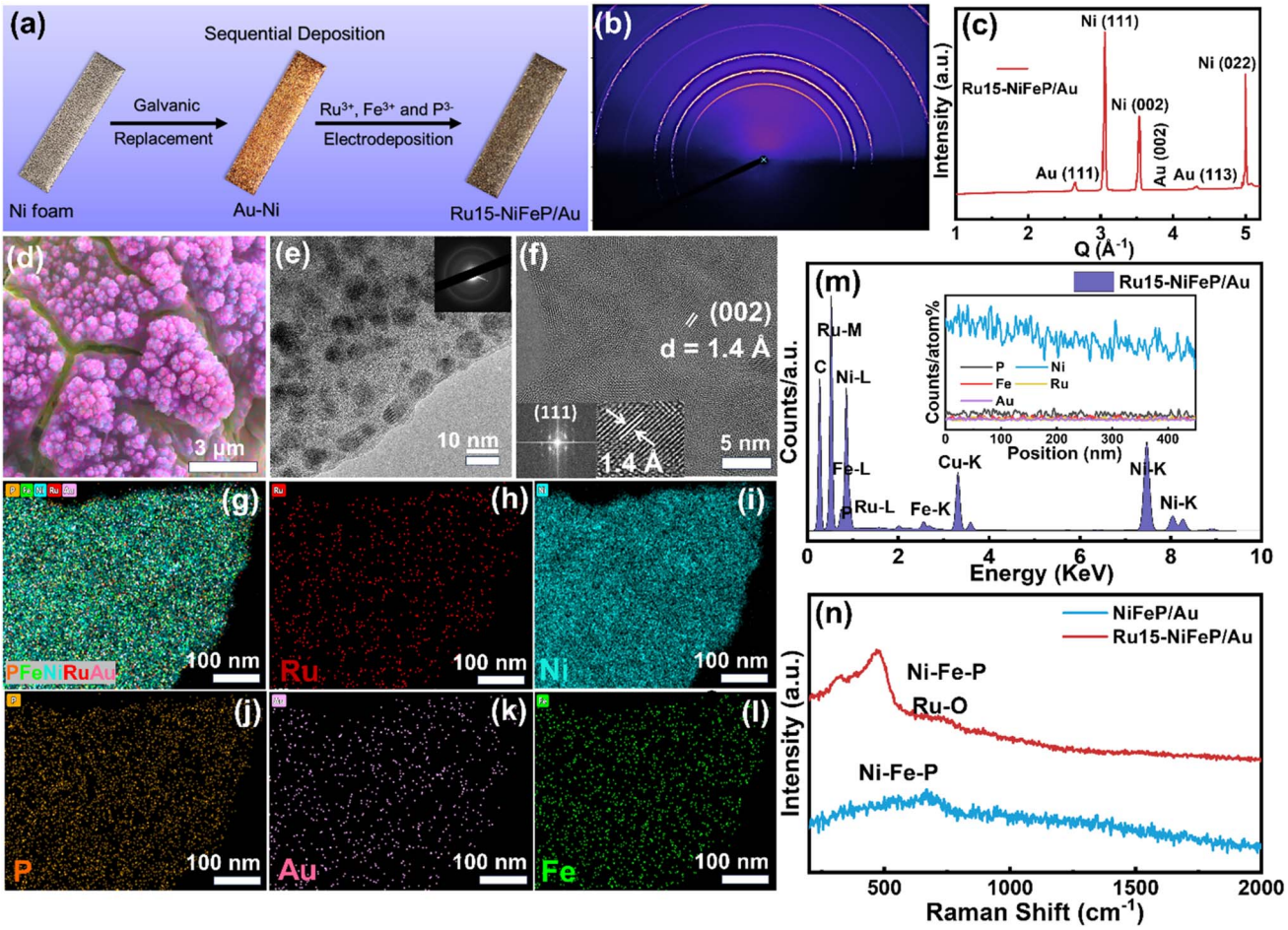

Fig. 1 (a) Schematic of the synthesis of Ru-NiFeP/Au catalysts. (b and c) Synchrotron-based WAXS 2D map and corresponding *Q*-values. (d) SEM elemental mapping color composite of Ru15-NiFeP/Au islands. (e) HRTEM images of Ru15-NiFeP/Au islands, with the SAED pattern in the inset. (f) High-magnification TEM image of Ru-NiFeP/Au, with the corresponding FFT in the inset. (g–l) EDS mapping results of the mix composite, Au, Ru, Fe, Ni, and P. (m) EDS spectra in STEM mode, with the EDS intensity profile in the inset. (n) Raman spectra of NiFeP/Au and Ru15-NiFeP/Au catalysts.

lattice fringes with 0.14 nm *d*-spacing corresponding to Au(002), while Ru15-NiFeP nano islands were largely amorphous with a short-range crystallinity and reflection originating from the underlying Au/Ni layers (Fig. 1e and f). The selected area electron diffraction (SAED) pattern in Fig. 1e inset shows the diffused ring pattern due to the amorphous nature, while the fast Fourier transform (FFT) of the image in Fig. 1f inset displays sharp diffraction spots due to the Au (111) plane, which is consistent with the XRD results.[43] HAADF-STEM elemental mapping of Ru15-NiFeP/Au further validated the homogeneous distribution of the constituting elements (Fig. 1g–l). The EDX spectrum and intensity profile in STEM mode confirmed the presence of Ru (0.64%), Fe (0.07%), Ni (14.26%), Au (0.03%), and P (0.51%) from the Ru-NiFeP/Au islands (Fig. 1m). The Raman spectra of NiFeP/Au and Ru-NiFeP/Au exhibited signature peaks centered between 300 and 700 cm^{-1}, corresponding to the Fe–P and Ru–O stretching vibrations, respectively (Fig. 1n).[39,45] The morphologies of Au-Ni and Ru15-NiFeP/Au at various magnifications are shown in Fig. S7–S8.†

To unravel the electronic and chemical composition, X-ray photoelectron spectroscopy (XPS) was conducted for the Au-Ni and Ru-NiFeP/Au materials. The XPS of Au-Ni in the Au4f region shows two peaks at 83.8 and 87.5 eV assigned to $4f_{7/2}$ and $4f_{5/2}$, respectively, indicating metallic Au (Fig. S9†).[41] The Ni2p peaks at 854.8 and 872.4 eV originating from the $2p_{3/2}$ and $2p_{1/2}$ transitions correspond to the +2 states of the surface oxidized Ni of the Ni foil.[41] The Ru3p core level spectrum of Ru-NiFeP/Au exhibited two peaks centered at 463.1 and 485.3 eV due to intermediate oxidation between Ru(0) and Ru(IV), respectively, while the peaks at 468.2 and 488.8 eV resulted from the Ru(IV) states (Fig. S10†).[31,42,46] For the Fe2p spectrum, the XPS peaks at 712 eV originated from $2p_{3/2}$ and those at 709.6, 711.4, and 713.9 eV are related to the +2, +3, and satellite peaks of Fe, respectively.[43] The Ni2p XPS spectrum of Ru-NiFeP/Au shows peaks at 854.3, 856.1, 872.3, and 874.6 eV, and are indexed to +2/+3 oxidation states.[47,48]

The Ni2p and Au 4f peaks of Ru-NiFeP/Au were shifted 0.5 and 0.2 eV, respectively, toward low BE value compared to Au–Ni, indicating the electronic coupling of Ru and Fe with Ni. The P2p spectrum shows peaks at 131.08 and 132.5 eV corresponding to the P^{3-} and PO_4^{3-} states.[28] The Ru3d spectrum shows the presence of the $Ru3d_{3/2}$ and $Ru3d_{5/2}$ states for the

$Ru^{\delta+}$ states.[31,42,46] The O1s core spectra display four peaks indexed to M–O, M–P, M–H_2O, and a shoulder peak at 528–532 eV for the surface adsorbed –OH, respectively.[28,43] XPS analysis for other concentrations of Ru in Ru-NiFeP/Au also demonstrated a similar pattern (Fig. S11†). The electronic nature and coordination environment of Ru15-NiFeP/Au were investigated using synchrotron-based soft X-ray absorption (sXAS) (TEY mode), X-ray absorption near-edge structure (XANES), and extended X-ray absorption fine structure (EXAFS) analyses. Fig. 2a and b show the Excitation-Emission Matrix Spectroscopy (EEMS) scanning profile for Ru15-NiFeP/Au. The EEMS scan clearly shows bright Ru M, Ni L (Fig. S12a†), P K (Fig. S12b†) and O K (Fig. S12c†) and Fe L edges; however, the Au edge cannot be detected due to the high energy of the Au L-edge compared to the energy range for soft X-rays (2000 keV). The Ru M-edge sXAS spectra of Ru15-NiFeP/Au displayed two signature peaks for the Ru M_{III} and Ru M_{II}-edges at 485.4 and 463.5 eV, suggesting $Ru^{\delta+} \leq 4+$ oxidation state (Fig. 2c).[49] The Fe L-edge spectra also show two peaks (Fe L_{III} and Fe L_{II}) at 720.9 and 709.4 eV for iron present in the 3+ oxidation state (Fig. 2d).[50] The Fe L_{II} edge displayed t_{2g} and e_g peak splitting, suggesting the presence of the O coordination iron species. Fig. 2a–d reveal that Ru15-NiFeP/Au contains $Ru^{\delta+} \leq 4+$ and Fe 3+ oxidation states, respectively. The Ni K-edge XANES spectra of NiO displayed the edge energy at around 8330.5 eV with a pre-edge feature, while the Ni foil was metallic. Therefore, a positive shift was observed for Ni in Ru15-NiFeP/Au, indicating the oxidized Ni in the material (Fig. S13†).[51] The Fe K-edge XANES spectra of Ru15-NiFeP/Au exhibited a sharp rising edge at 7115.6 eV, along with a pre-edge feature similar to that reported for γ-FeOOH or Fe_2O_3, corroborating the 3+ octahedral (O_h) environment for the Fe species.[52] Furthermore, the Fe K-edge energy of Ru15-NiFeP/Au was present at relatively high energy compared to Fe_2O_3 (Fe^{3+}), signifying the electron deficient

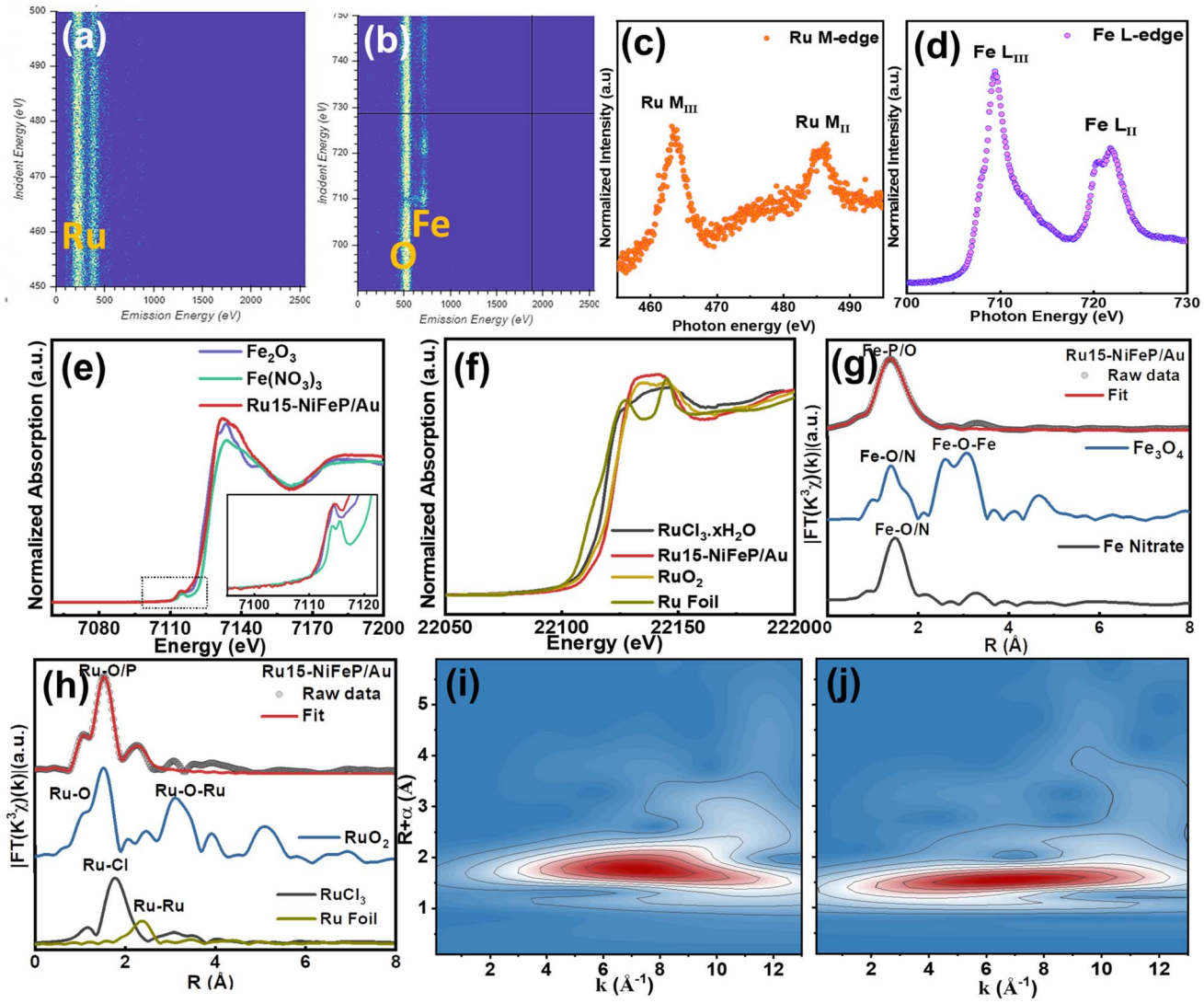

Fig. 2 Synchrotron-based soft and hard X-ray absorption spectra of the Ru15-NiFeP@Au islands. (a) and (b) EEMS scanning profiles of Ru and Fe. (c) and (d) Corresponding soft XAS spectra for the Ru M-edge and Fe L-edge. (e) and (f) Fe K-edge and Ru L-edge XANES spectra (dots–raw data and lines–fitted data). (g) and (h) FT-EXAFS spectra of Ru and Fe. (i) and (j) Ru WT EXAFS map of $RuCl_3$ and Ru15-NiFeP@Au.

under-coordinated Fe species (Fig. 2e).[53] The difference between Fe_2O_3 and Ru15-NiFeP/Au is related to a change in coordination in the latter. The increased white line intensity for Ru15-NiFeP/Au further strengthens the assumption of a partial charge transfer from Fe3d → O2p.[53] The Ru K-edge XANES spectra also displayed a similar enhancement in the white line peak intensity due to the undercoordinated state (Fig. 2f).[42] The Fourier transform (FT) Fe-EXAFS spectra of Ru15-NiFeP/Au show an intense first shell scattering at 1.39 Å, originating from the Fe–P/O coordination. The presence of weak scatterings features at higher *R* values (2.66 and 3.29 Å) originated from the Fe–O–Fe and Fe–O–Ru coordination, suggesting partial oxidation of the Fe–P species (Fig. 2g).[52,53] The EXAFS data fitting of Ru15-NiFeP/Au, considering the presence of the Fe–P/Fe–O coordination, demonstrated a Fe–P/Fe–O bond length of 2.34/1.90 Å with a coordination number of 4.4/4.5 (Table S1†). The lower CN values of Fe–P/Fe–N in Ru15-NiFeP/Au compared to that of the crystalline FeP and Fe–O (Fe_3O_4) structures suggest that the undercoordinated species probably originated from the unfulfilled coordination in the amorphous structure. The Ru EXAFS spectra of Ru15-NiFeP/Au shows peak features that are significantly different from those of RuO_2 and $RuCl_3$. The Ru–O/P scattering was observed at low R values compared to $RuCl_3$, suggesting the successful transformation of ruthenium chloride to phosphide. Additionally, the Ru–O–Ru peak for the RuO_2 state was absent, indicating that the Ru–O sites were not present in the oxide. Furthermore, no peak features corresponding to metallic Ru were observed, indicating that Ru was bonded with P/O (Fig. 2h).[42,46] The fitting of EXAFS gives Ru–O, Ru–P and Ru–Fe bond lengths of 1.92, 2.03 and 2.59 Å, and R values with a CN of 1.3, 4.6 and 6.9, respectively. The *R*-values for Ru and Fe in EXAFS show that the coordination lengths of Ru–O and Fe–O were slightly shifted at higher value due to the introduction of the Ru–Fe–P species in Ru-NiFeP/Au.[42,53] The Wavelet Transform (WT) EXAFS map of Ru for Ru15-NiFeP@Au and $RuCl_3$ was further acquired to understand the coordination environment (Fig. 2i and j). The Ru WT EXAFS map for Ru15-NiFeP@Au displayed a sharp bright zone centered at $K = 7.37$ $Å^{-1}$ and $R = 1.77$ Å, originating from Ru–P/O scattering. These scatterings were quite different from those of $RuCl_3$ ($K = 7.02$ $Å^{-1}$ and $R = 1.56$ Å), suggesting the complete transformation of $RuCl_3$ to Ru–P during electrocatalytic synthesis. A very faint zone in the WT map of Ru15-NiFeP@Au at $K = 10.98$ $Å^{-1}$ and $R = 2.47$ Å was assigned to an extremely small contribution of Ru–Fe/Ru–P–Ru scattering.

Electrocatalytic OER assessment of Ru-NiFeP/Au

The electrochemical OER activity of the electrodes was assessed in an O_2-saturated three-electrode setup in 1 M KOH. Initially, polarization studies were conducted at 5 mV s^{-1} and the backward CV response is provided to exclude any capacitive interference, as shown in Fig. 3a. Among the different electrodes, Ru15-NiFeP/Au exhibited outstanding activity, exhibiting low overpotentials (η) of 223 and 256 mV at current densities (j) of 10 and 100 mA cm^{-2}, respectively. Other variants required comparatively higher overpotentials [*e.g.*, Ru5-NiFeP/Au (242 mV), Ru25-NiFeP/Au (254 mV), NiFeP/Au (284 mV), NiFeP/Ni (287 mV), Au–Ni (314 mV), and pristine Ni (410 mV)] to deliver 10 mA cm^{-2}. The carrier migration is well enriched by suppressing the Ni^{2+} to Ni^{3+} oxidation behavior on the RuFeP sites compared to only Ni, as evidenced by the positive steep increase in the current.[16,54] The nature of the charge transport phenomenon derived from log j *versus* η and the low Tafel slope of 32 mV dec^{-1} obtained for Ru15-NiFeP/Au infers a $4e^-$ transfer process. Meanwhile, others showed high Tafel values (Fig. 3b), Ru5-NiFeP/Au (47 mV dec^{-1}), Ru25-NiFeP/Au (35 mV dec^{-1}), NiFeP/Au (68 mV dec^{-1}), NiFeP/Ni (55 mV dec^{-1}), Au–Ni (120 mV dec^{-1}) and pristine Ni (132 mV dec^{-1}), indicating lower charge transport kinetics. The charge transfer resistance (R_{ct}), representative of the electron transfer ability of the electrodes, was measured *via* EIS at 400 mV *vs.* RHE from the fitted electric equivalent circuit (EEC). From Fig. 3c, the R_{ct}, measured using the corresponding equivalent circuit (inset), steadily decreased from pristine Ni (2.53 Ω), Au–Ni (2.01 Ω), and NiFeP/Au (0.752 Ω) to Ru15-NiFeP/Au (0.29 Ω), with the lowest semicircle. This agrees with the polarization studies and the sharp rise in current for Ru15-NiFeP/Au, signifying greater carrier migration. A comparison of the state-of-the-art RuO_2 is shown in Fig. S14.† The electrochemical active surface area (ECSA) for the catalysts was measured from the double-layer capacitance (C_{dl}) (Fig. S15†). As shown in Fig. S15,† Ru15-NiFeP/Au showed a lesser slope value (7.6 mF cm^{-2}) compared to Au–Ni (14.53 mF cm^{-2}). This directly demonstrates the improved charge migration across the interface and the capacitance in Au–Ni being linked to the superior 'electrophilic nature of Au'.[41] Furthermore, the intrinsic specific activity from the ECSA normalized LSVs indicate the improved OER performance for the Ru15-NiFeP/Au islands, as depicted in Fig. 3d. The calculated TOF values at the potential intervals (Fig. 3e) showed that Ru15-NiFeP/Au delivers better O_2 turnover (0.012 S^{-1} at 1.7 V). Ru15-NiFeP/Au delivered a high mass activity of 408 A g^{-1} at 1.7 V (Fig. 3f). This is attributable to the surface reconstruction enabling lesser active species results in low loading and improved mass activity.[55] The OER performance of Ru15-NiFeP/Au is superior to many other related effective electrodes in terms of the overpotential (η_{10}) and Tafel slope, as shown in Fig. 3g.[56–64] A comparison of the catalytic performance of Ru15-NiFeP/Au with various phosphide catalysts is also tabulated in Table S2.† LSVs at different pH values of 12, 13, and 14 were analyzed to understand the onset potential of Ru15-NiFeP/Au. As shown in Fig. 3h, a linear decrease in the onset potential with increasing pH signifies the population of OH^- ions at the electrode/electrolyte interface. The electrochemical stability of Ru15-NiFeP/Au was tested under potentiodynamic and potentiostatic conditions. The LSV study performed before and after cycling, as shown in Fig. S16,† demonstrates the high stability with minimum degradation. Furthermore, a constant current density of 100 mA cm^{-2} is retained with very low decrement in activity for 100 h, suggesting the superior stability of the Ru15-NiFeP/Au islands (Fig. 3i).[26,27] To unveil the catalyst robustness stability, post-OER characterizations such as SEM with mapping (Fig. S17†), HR-TEM (Fig. S18†) and XPS (Fig. S19†) analyses were carried out. The SEM images showed the retained

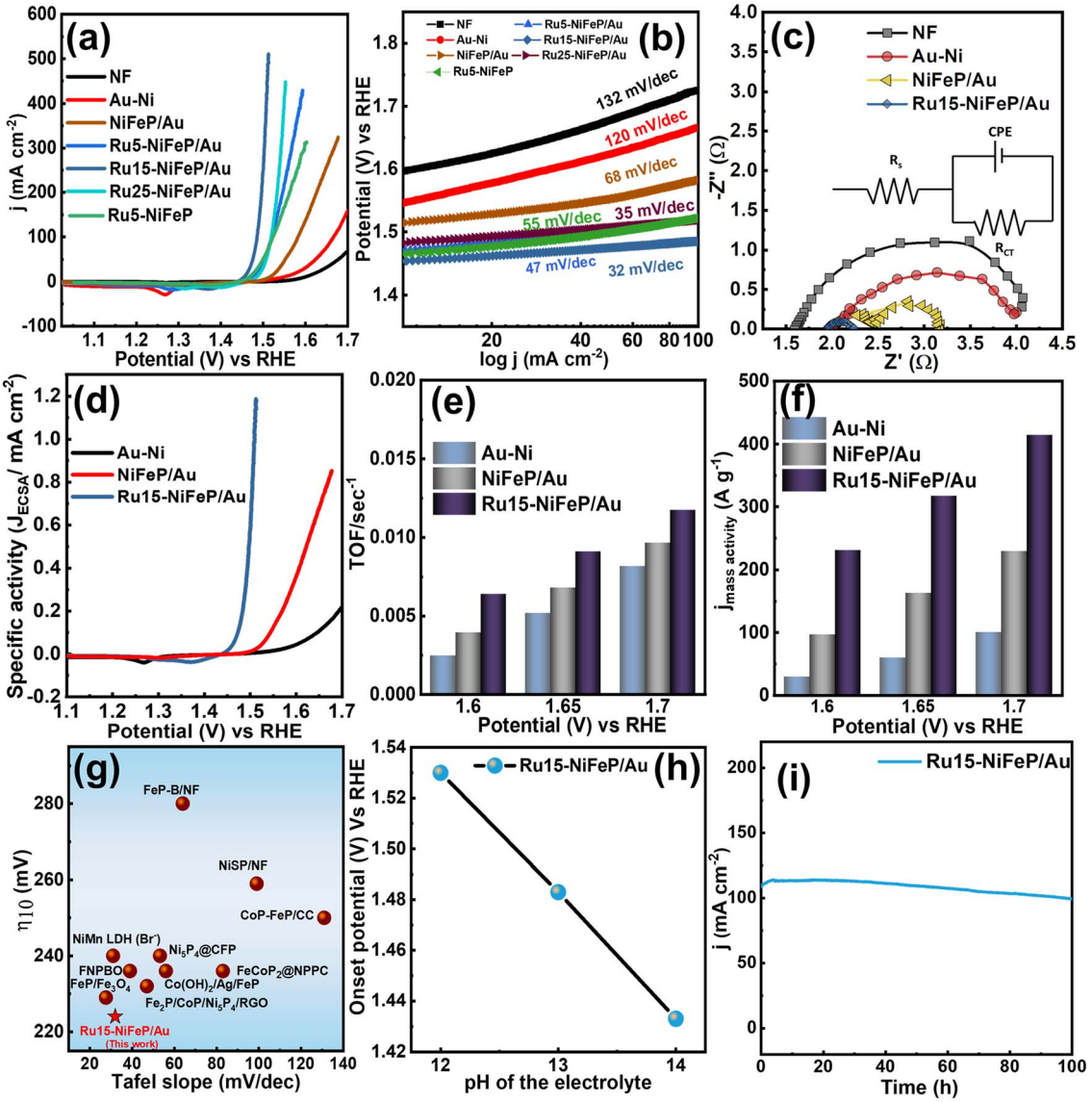

Fig. 3 Electrocatalytic OER performance of the electrodes. (a) Backward cyclic voltammetry (CV) curves in 1 M KOH at a scan rate of 5 mV s^{-1}. (b) Corresponding Tafel slopes. (c) EIS at 400 mV overpotential. Inset showing the Randle circuit obtained after fitting the EIS curve. (d) Specific activity. (e) Turn over frequency. (f) Mass activity. (g) Comparison of the overpotential and Tafel slope with literature. (h) Onset potential *versus* pH effect on Ru15-NiFeP@Au-Ni. (i) Potentiostatic stability of Ru15-NiFeP@Au-Ni for 100 h in 1 M KOH.

structural features of the Ru15-NiFeP/Au islands, and the mapping results confirmed the presence of Au, Ni, Fe, Ru, and P. The HR-TEM images demonstrate the Ru-NiFeP islands after harsh anodic conditions, indicating the substantial stability of the catalyst. The XPS high-resolution spectra of the Ru 3d, Ni 2p, Fe 2p, and P 2p demonstrate the stability and show the oxidized forms of the catalyst surface that occur due to the RuO_x, Ni and Fe oxy-hydroxides, which is usually formed under anodic overpotentials in KOH.[26,27]

Dynamic spectroelectrochemical investigations on electrocatalysts with *in situ* EIS and *in situ* SERS analyses

The *in situ* EIS method is an important tool that can be used to elucidate details on the adsorption and desorption of intermediates at the electrode/electrolyte interface.[65] *In situ* EIS between 1.3–1.6 V with 50 mV potential interval was performed on Au–Ni, NiFeP/Au, and Ru15-NiFeP/Au to assess the kinetics of the O-intermediates on the metal active sites and the resulting electrical conductivity, as depicted in Fig. 4a–c. The *iR*-uncorrected CV from 1.3–1.6 V chosen for EIS is given in Fig. S20,† where the chosen region couples the oxidation of the Ni^{2+}/Ni^{3+}, Fe^{2+}/Fe^{3+} states and concomitant OER. The Nyquist plots revealed the trends in the O-intermediate kinetics with a semicircle arc from 1.3–1.6 V, which were significantly reduced with increasing potentials, showing the alleviated O-adsorption for a faster charge transport. Among them, the Ru15-NiFeP/Au islands delivered improved electrical conductivity due to the abrupt adsorption of the O-intermediates. The

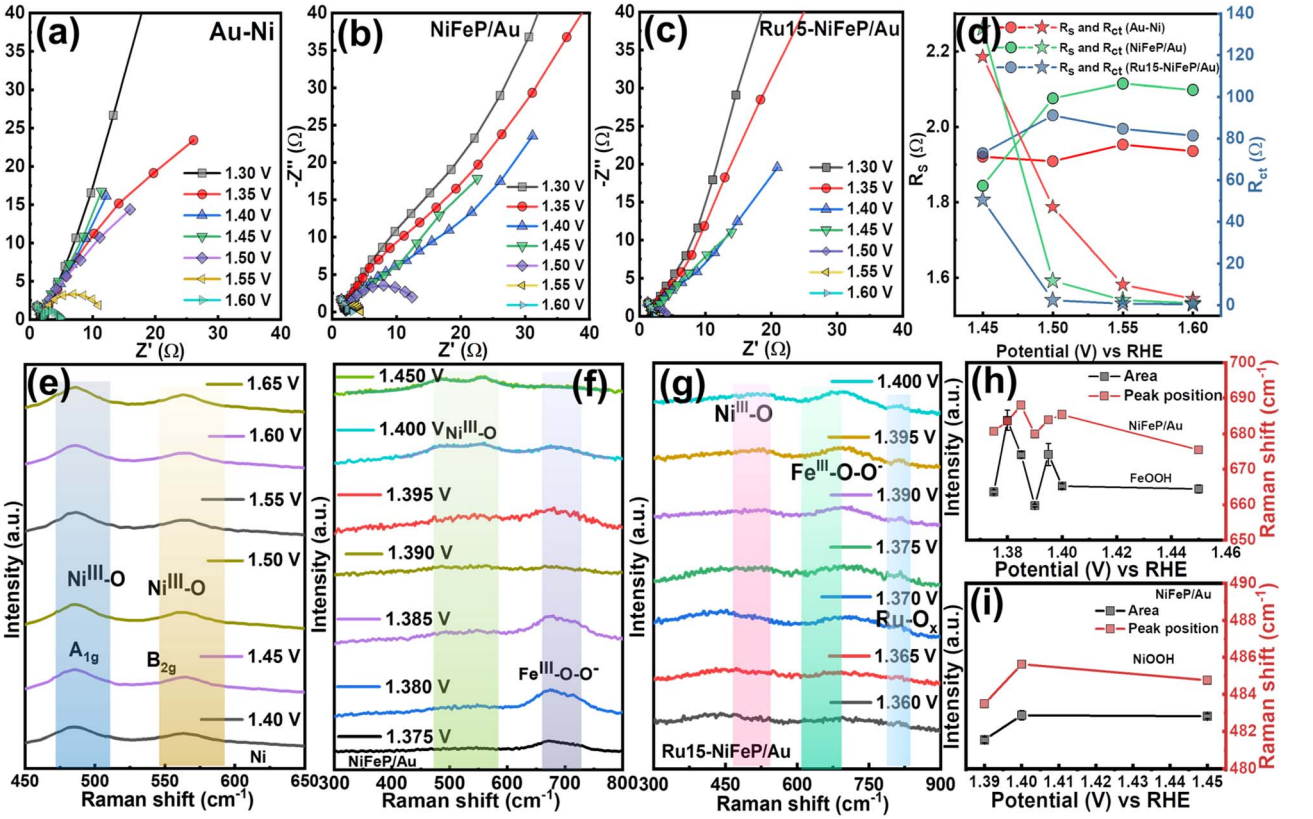

Fig. 4 *In situ* EIS and *in situ* SERS results. (a–c) *In situ* EIS spectral studies of Au–Ni, NiFeP/Au, and Ru15-NiFeP/Au at varying potential intervals from 1.3 to 1.6 V. (d) Comparison of fitted R_s and R_{ct} values for Au-Ni, NiFeP/Au, and Ru15-NiFeP/Au.ues (e) *In situ* SERS studies on Ni foam from 1.4 to 1.65 V with a 50 mV potential interval. (f and g) *In situ* SERS results of NiFeP/Au and Ru15-NiFeP/Au islands with 5–10 mV potential interval. (h and i) Area and peak position difference in NiFeP/Au for NiOOH A_{2g} and FeOOH peaks.

EEC was fitted from 1.45–1.6 V, and the resultant R_s and R_{ct} values are shown in Fig. 4d. The OER process at this region is completely charge transfer-controlled. From a closer look at Au–Ni in Fig. S20,† the potential is exploited more for the oxidation current in the oxidation of Ni^{2+}/Ni^{3+}. The O-intermediate charge transport is suppressed, agreeing with the EIS results with the increased semicircle arc. In the case of NiFeP/Au and Ru15-NiFeP/Au islands, the oxidation current for the Ni^{2+}/Ni^{3+}, Fe^{2+}/Fe^{3+} states are suppressed. The applied potential is mainly used for charge transport, and the O-intermediate adsorption is facile for Ru15-NiFeP/Au with improved charge transport (Fig. 4d).[66] These results match nicely with the polarization studies given in Fig. S20,† where the oxidation and OER currents are varied, and the oxidation currents are mainly reduced after coupling the Ru15-NiFeP/Au islands with the faster O-intermediate adsorption. To further investigate the nature of the actual active sites under the applied potential regime, *in situ* SERS studies were carried out in 1 M KOH under varying potential intervals.[38,39] SERS studies mainly require Au, Ag, or Cu as coinage metals to intensify the signals of the surface adsorbed species that are relatively low in concentration and exhibit short lifetimes during OER.[39] In NiFe systems, the role of the active sites was previously investigated by Cejun *et al.* with the Au plasmonic core for SERS.[38] Interestingly, it was found that Fe atoms are the preliminary sites for the oxidation of OH^- to $O–O^-$ at lower overpotentials, and that Ni^{III} acted as a site for oxidation of $O–O^-$ to O_2 at higher overpotentials. It was affirmed that FeOOH acts as a real active site at low bias, while NiOOH catalyzes O_2 evolution at high bias, yielding a 'dual metal synergistic mechanism' in the Ni–O–O–Fe structure.[38] Based on these findings, initially, Ni foam is chosen as a substrate and *in situ* SERS studies were performed between 1.4–1.65 V at 50 mV interval (Fig. 4e). As shown in Fig. S20,† under OCP and until 1.35 V, no peaks evolved, suggesting that there was no oxidation. At 1.4 V, two new peaks were observed at 465 and 584 cm^{-1}, corresponding to the A_{1g} and B_{2g} modes from Ni^{III}–O stretching in NiOOH.[38] These peaks were enhanced with increasing potentials, and started to fade at high overpotentials above 1.65 V due to the bubble formation that interferes with exposure to the laser beam (Fig. 4e). The Lorentzian fitting of Ni is shown in Fig. S21,† and the peak position and areas were plotted as a function of the applied potential. To elucidate the nature of the active species in NiFeP/Au, SERS studies were carried out under OCP, from 1.35 to 1.45 V at 5 mV intervals in the lower potential range to identify the precise changes (Fig. 4f).

For NiFeP/Au, there was no increase in the peak intensity observed until 1.375 V. At 1.38 V, a new peak corresponding to the FeOOH sites for O–O bond formation was observed. At 1.4 V and above, a new Ni^{3+} peak appeared for NiOOH, which acted as

an 'active site' for O_2 desorption at the surface.[28,38,67] From these observations, it is affirmed that the Ni–O–O–Fe sites are essential for OER and at low overpotentials. Fe is the 'active site' for adsorbing the hydroxides. At higher overpotentials, Ni^{3+} offers a fast generation of O_2 molecules.[38] Furthermore, the prepared M–P surface changed to oxides/oxyhydroxides during OER and acted as 'real active sites'. This SERS observation reveals how the presence of both Fe and Ni controls the O_2 formation. The Lorentzian fitting of NiFeP/Au (Fig. 4h) shows that the peak for FeOOH increases in intensity at 1.38 V and fades at higher bias, whereas the NiOOH peak intensity is enhanced after 1.4 V (Fig. 4i). In the case of Ru15-NiFeP/Au, Ru–O peaks are observed in addition to the peaks for NiOOH and FeOOH (Fig. 4g). This indicates the formation of Ru–O bonding over Ni–Fe–O–O–H, which alters the local charge distribution near the surface in high alkaline conditions.[39,46] The Lorentzian fitting of the peak position and area is depicted in Fig. S22.† In the Ru15-NiFeP/Au islands, Ru ensures a high-rate of activity, and the presence of Ru–O bonds for the M(4d)–O(2p) synergism improves the catalytic activity of the NiFe-oxyhydroxide surface.[68]

Computational mechanistic studies on Ru15-NiFeP/Au

A schematic representation of the plausible electron transfer pathways is depicted in Fig. 5a, which portrays the electron transport with increased electrical conductivity in amorphous catalysts.[68] The doping of Ru over FeP resulted in a decrease in the band gap, thus inducing a facile electron transfer, as shown in the histogram for FeP and RuFeP (Fig. 5b).[68] The optical band gap calculated using the Tauc plot for FeP and RuFeP was found to be 2.34 eV and 1.56 eV, respectively, validating the band gap reduction (Fig. S23a and b†). Furthermore, water contact angle studies (Fig. 5c) demonstrated the superhydrophilic wettability of Ru15-NiFeP/Au compared to pristine NF (water contact angle 120°), which is expected to contribute towards the high catalytic activity in OER. This 'superhydrophilicity' was prompted from the conducting/hydrophilic P^{3-} ions and PO_4^{3-} groups in the bulk.[44] *In situ* SERS studies confirm that NiFeOOH/RuO are the active sites on which the O-intermediates turn into O_2 molecules. Thus, we performed DFT calculations for RuO over the NiFe-OOH system to understand the OER mechanism on this catalyst. It is well known that the nature of the active sites on the surface can significantly impact the adsorption energy of the intermediates.[69,70] The surface of NiFe-OOH has two types of oxygen. The type-1 configuration shows an active site where the surface oxygen is connected to two Ni atoms and one Fe atom, whereas the type-2 configuration shows the surface oxygen connectivity with two Fe atoms and one Ni atom (Fig. S24 and S25†). After identifying the two non-equivalent sites over the NiFe-OOH surface, the RuO unit is incorporated above the Fe atom and named as type-1 RuO/NiFe-OOH, and above the Ni atom as type-2 RuO/NiFe-OOH (Fig. S26 and S27†). The OER pathways in type-1 NiFe-OOH and type-2 NiFe-OOH are shown in Fig. S28,† and the OER pathways in type-1 RuO/NiFe-OOH and type-2 RuO/NiFe-OOH are provided in Fig. 5d and e. At $U = 0$ V, the Gibbs free energy is ascending from *OH to *OOH for all four systems (Fig. 5f, g and S29†). For type-1 NiFe-OOH, the potential limiting step is *OH formation and adsorption on the surface-active site since the ΔG value is maximum for this step, *i.e.*, 1.94 eV. However, for type-2 NiFe-OOH, the potential limiting step is deprotonation of *OH to *O with a ΔG value of 1.82 eV. The onset potential has been reduced from type-1 to type-2 NiFe-OOH by a magnitude of 0.12 V. This change in magnitude can be attributed to the difference in the chemical environment of surface oxygen. For the type-2 case, the overall OER activity has been enhanced because of the presence of two Fe atoms. The Fe atom induces ionic character in the Fe–O bond, which helps in better absorption of the intermediates. This observation agrees with the *in situ* SERS results, where the O-intermediate adsorption is facile in FeOOH sites. However, for the Ni atom, the increased covalency in the Ni–O makes it relatively poor against OER activity.[47] At the theoretical onset potential of OER, *i.e.*, 1.23 V, both type-1 and type-2 NiFe-OOH exhibit ascending free energy until the *O intermediate and then descending until O_2. However, the ΔG values for the PLS of type-1 and type-2 at the theoretical onset potential are 0.71 eV and 0.58 eV, respectively. Hence, to make the reaction spontaneous, an onset potential of 1.94 V must be applied for type-1 NiFe-OOH and 1.82 V for type-2 NiFe-OOH. To better understand the charge transfer, a Bader charge analysis was performed.

For the *OH intermediate, the charge transfer from Fe to O at the active site is 0.17 units more than the charge transfer from Ni to O at the active site, further confirming the role of Fe as preliminary active sites in OER (Tables S3–S6†). Additionally, the charge separation between the O and H of *OH is less for the case of type-2 NiFe-OOH. The deprotonation step for the same becomes difficult compared to type-1. Therefore, the potential limiting step for type-2 NiFe-OOH is deprotonation of *OH to *O. Furthermore, the *OOH intermediate is weakly adsorbed on the surface for both cases (Fig. S25†). The presence of the RuO unit over NiFe-OOH has shown a significant reduction in the overpotential of OER. The oxyhydroxide intermediate is stable on the surface when Ru is the active site on RuO/NiFe-OOH (Fig. 5d and e). The type-1 RuO/NiFe-OOH requires 1.58 V for the formation of the oxyhydroxide intermediate. On the other hand, for type-2 RuO/NiFe-OOH, the formation of O_2 from OOH requires 1.70 V (Fig. 5f and g). At $U = 0$ V, the free energy change for both cases is positive and ascending. At 1.23 V, the theoretical overpotential of water splitting, the ΔG values of all intermediates are negative unlike type-1 and type-2 NiFe-OOH (Tables S7–S10†). Both type-1 and type-2 RuO/NiFe-OOH perform better than the bare NiFe-OOH surfaces. Ru in RuO/NiFe-OOH acts as the active site because of the availability of the uncoordinated sites on the Ru atom, which is supported with the XANES results (Fig. 2). In addition, Ru atoms can provide electrons more readily to the intermediates than surface oxygen. To make the whole reaction spontaneous, theoretical overpotentials of 0.35 V and 0.47 V have to be supplied for type 1 RuO/NiFe-OOH and type-2 RuO/NiFe-OOH, respectively. Here, the synergistic effect of the Fe atom can be seen in RuO/NiFeOOH. The theoretical overpotential of type 1 RuO/NiFe-OOH is 0.12 V lower in magnitude than that of type 2

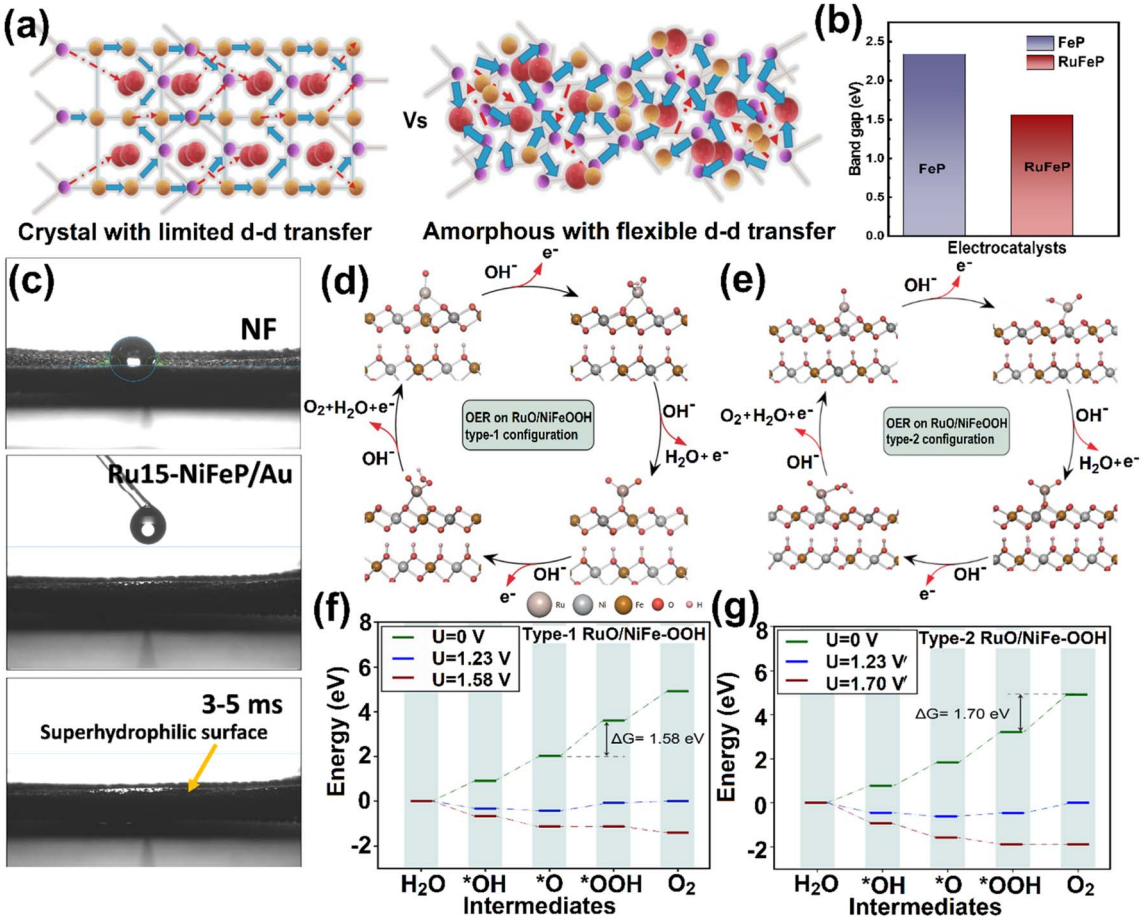

Fig. 5 (a) Electronic structure of crystalline and amorphous RuFeP islands. (b) Band gap of the FeP and RuFeP electrocatalysts. (c) Superhydrophilic nature of Ru15-NiFeP/Au islands, on which the water droplet falls in immediately within 3–5 ms. (d) OER on the RuO/NiFeOOH type-1 configuration. (e) OER on the RuO/NiFeOOH type-2 configuration. (f) OER free energy profile on the RuO/NiFeOOH type-1 configuration and (g) OER free energy profile on the RuO/NiFeOOH type-1 configuration.

RuO/NiFe-OOH. In this study, the minimum overpotential of 0.35 V towards OER was observed in type-1 RuO/NiFe-OOH. From the overall studies, the presence of NiFe-oxyhydroxides with the RuO surface ensured fast electron transfer towards OER, and can be extended to other catalytic applications.

Conclusions

In summary, we have developed a highly active and stable OER catalyst comprising Ru-NiFeP/Au islands with optimized Ru loading that showcase very low overpotential (η_{10}: 223 mV) and Tafel slope (32 mV dec^{-1}). *In situ* SERS studies demonstrated that the presence of Ru synergistically improves the performance, with FeOOH sites acting as a promoter at lower bias for –OH adsorption and NiOOH being the active sites at higher bias, for O_2 desorption. From DFT, it is confirmed that the FeOOH sites induce ionic character in the Fe–O bond for the facile absorption of the O-intermediates. DFT studies further concluded that the presence of Ru–O coordination to the NiFeOOH sites could drastically improves the activity by diminishing the free energy barrier of 0.12 eV for the OER rate-determining step. Also, amorphization gives rise to 'dangling bonds' on the surface to induce better charge transport, as reflected in the faster kinetics. Overall, we demonstrated that the TMPs surface with noble metals like Ru can optimize the OER performance, and the Au surface for SERS can provide a deeper understanding of the active sites during OER. The findings will reinforce research studies in the design of stable and active TMPs-based OER catalysts, and those employing SERS to understand the nature of the active site.

Data availability

All data that support the findings of this study are provided within the paper, and its ESI† files and are also available from the corresponding author upon request.

Author contributions

K. K. planned and prepared the electrodes, carried out the experiments and wrote the manuscript. P. K. helped with XRD, XPS, sXAS, and XANES data analysis and helped in planning electrochemical measurements. P. G. performed the DFT studies. S. R. provided HRTEM, XPS characterizations, and

edited the manuscript. H. S. S. performed *in situ* Raman studies and A. S. Z. helped with SEM analysis. S. K. N., A. A. B. and M. M. collected contact angle measurements and performed XRD analysis data. G. S., A. K. S., P. M. A., S. R. and M. G. K. supervised the research and edited the manuscript.

Conflicts of interest

There are no conflicts of interest to declare.

Acknowledgements

The authors would like to acknowledge the financial support by the Canada First Research Excellence Fund (CFREF) at the University of Calgary. Part of the research described in this paper was performed at the Canadian Light Source (project: 35G12344), a national research facility of the University of Saskatchewan, which is supported by the Canada Foundation for Innovation (CFI), the Natural Sciences and Engineering Research Council (NSERC), the National Research Council (NRC), the Canadian Institutes of Health Research (CIHR), the Government of Saskatchewan, and the University of Saskatchewan. S. R. acknowledges support from IIT Kanpur (Project No.: 2024098) and the Chandrakanta Kesavan Centre for Energy Policy and Climate Solutions (Project No.: 2021136H). S. K. acknowledges SEED grant from Kalasalingam Academy of Research and Education. Drs Ning Chen, Beatriz Diaz-Moreno, Jay Dynes, Tom Regier and Zachary Arthur are kindly acknowledged for their help with the hard/soft X-ray and GI-WAXS analysis.

References

1 H. Ding, H. Liu, W. Chu, C. Wu and Y. Xie, *Chem. Rev.*, 2021, **121**, 13174–13212.
2 M. R. Nellist, F. A. L. Laskowski, J. Qiu, H. Hajibabaei, K. Sivula, T. W. Hamann and S. W. Boettcher, *Nat. Energy*, 2018, **3**, 46–52.
3 H. Mistry, A. S. Varela, S. Kühl, P. Strasser and B. R. Cuenya, *Nat. Rev. Mater.*, 2016, **1**, 1–15.
4 W. Tong, M. Forster, F. Dionigi, S. Dresp, R. Sadeghi Erami, P. Strasser, A. J. Cowan and P. Farràs, *Nat. Energy*, 2020, **5**, 367–377.
5 H. Over, *ACS Catal.*, 2021, **11**, 8848–8871.
6 S. Anantharaj, S. R. Ede, K. Sakthikumar, K. Karthick, S. Mishra and S. Kundu, *ACS Catal.*, 2016, **6**, 8069–8097.
7 P. Kumar, K. Kannimuthu, A. S. Zeraati, S. Roy, X. Wang, X. Wang, S. Samanta, K. A. Miller, M. Molina, D. Trivedi, J. Abed, M. A. Campos Mata, H. Al-Mahayni, J. Baltrusaitis, G. Shimizu, Y. A. Wu, A. Seifitokaldani, E. H. Sargent, P. M. Ajayan, J. Hu and M. G. Kibria, *J. Am. Chem. Soc.*, 2023, **145**, 8052–8063.
8 R. Subbaraman, D. Tripkovic, K.-C. Chang, D. Strmcnik, A. P. Paulikas, P. Hirunsit, M. Chan, J. Greeley, V. Stamenkovic and N. M. Markovic, *Nat. Mater.*, 2012, **11**, 550–557.
9 Y. Sun, H. Liao, J. Wang, B. Chen, S. Sun, S. J. H. Ong, S. Xi, C. Diao, Y. Du, J. O. Wang, M. B. H. Breese, S. Li, H. Zhang and Z. J. Xu, *Nat. Catal.*, 2020, **3**, 554–563.
10 A. Grimaud, O. Diaz-Morales, B. Han, W. T. Hong, Y. L. Lee, L. Giordano, K. A. Stoerzinger, M. T. M. Koper and Y. Shao-Horn, *Nat. Chem.*, 2017, **9**, 457–465.
11 S. Lee, K. Banjac, M. Lingenfelder and X. Hu, *Angew. Chem., Int. Ed.*, 2019, **58**, 10295–10299.
12 L. Zhang, Q. Fan, K. Li, S. Zhang and X. Ma, *Sustainable Energy Fuels*, 2020, **4**, 5417–5432.
13 H. Wang, K. H. L. Zhang, J. P. Hofmann, V. A. de la Peña O'Shea and F. E. Oropeza, *J. Mater. Chem. A*, 2021, **9**, 19465–19488.
14 N. Zhang and R. Jiang, *Chempluschem*, 2021, **86**, 1586–1601.
15 J. Kang, X. Qiu, Q. Hu, J. Zhong, X. Gao, R. Huang, C. Wan, L. M. Liu, X. Duan and L. Guo, *Nat. Catal.*, 2021, **4**, 1050–1058.
16 P. Zhai, M. Xia, Y. Wu, G. Zhang, J. Gao, B. Zhang, S. Cao, Y. Zhang, Z. Li, Z. Fan, C. Wang, X. Zhang, J. T. Miller, L. Sun and J. Hou, *Nat. Commun.*, 2021, **12**, 1–11.
17 F. Wang, Y. Zhang, J. Zhang, W. Yuan, Y. Li, J. Mao, C. Liu, C. Chen, H. Liu and S. Zheng, *ACS Sustain. Chem. Eng.*, 2022, **10**, 5976–5985.
18 M. S. Burke, L. J. Enman, A. S. Batchellor, S. Zou and S. W. Boettcher, *Chem. Mater.*, 2015, **27**, 7549–7558.
19 W. Ma, R. Ma, C. Wang, J. Liang, X. Liu, K. Zhou and T. Sasaki, *ACS Nano*, 2015, **9**, 1977–1984.
20 N. Mahmood, Y. Yao, J. W. Zhang, L. Pan, X. Zhang and J. J. Zou, *Adv. Sci.*, 2018, **5**, 1700464.
21 S. Dutta, A. Indra, Y. Feng, T. Song and U. Paik, *ACS Appl. Mater. Interfaces*, 2017, **9**, 33766–33774.
22 X. Xia, L. Wang, N. Sui, V. L. Colvin and W. W. Yu, *Nanoscale*, 2020, **12**, 12249–12262.
23 A. T. Swesi, J. Masud and M. Nath, *Energy Environ. Sci.*, 2016, **9**, 1771–1782.
24 A. Dutta and N. Pradhan, *J. Phys. Chem. Lett.*, 2017, **8**, 144–152.
25 Z. Pu, T. Liu, I. S. Amiinu, R. Cheng, P. Wang, C. Zhang, P. Ji, W. Hu, J. Liu and S. Mu, *Adv. Funct. Mater.*, 2020, **30**, 1–23.
26 Y. Shi, M. Li, Y. Yu and B. Zhang, *Energy Environ. Sci.*, 2020, **13**, 4564–4582.
27 W. Li, D. Xiong, X. Gao and L. Liu, *Chem. Commun.*, 2019, **55**, 8744–8763.
28 P. F. Liu, X. Li, S. Yang, M. Y. Zu, P. Liu, B. Zhang, L. R. Zheng, H. Zhao and H. G. Yang, *ACS Energy Lett.*, 2017, **2**, 2257–2263.
29 P. Yan, Q. Liu, H. Zhang, L. Qiu, H. Bin Wu and X. Y. Yu, *J. Mater. Chem. A*, 2021, **9**, 15586–15594.
30 S. Sultan, M. Ha, D. Y. Kim, J. N. Tiwari, C. W. Myung, A. Meena, T. J. Shin, K. H. Chae and K. S. Kim, *Nat. Commun.*, 2019, **10**, 1–9.
31 D. Chen, Z. Pu, R. Lu, P. Ji, P. Wang, J. Zhu, C. Lin, H. W. Li, X. Zhou, Z. Hu, F. Xia, J. Wu and S. Mu, *Adv. Energy Mater.*, 2020, **10**, 1–10.
32 Z. Xu, X. Zhang, X. Wang, J. Fang, Y. Zhang, X. Liu, W. Zhu, Y. Yan and Z. Zhuang, *ACS Nano*, 2021, **15**, 7131–7138.

33 N. Li, L. Mao, Y. Fu, H. Wang, Y. Shen, X. Zhou, Q. Li and J. Qian, *Inorg. Chem. Front.*, 2024, 8139–8145.
34 J. Chen, J. Liu, S. Xu, Y. Wu, Y. Ye and J. Qian, *Inorg. Chem. Front.*, 2024, **11**, 4876–4885.
35 D. Chen, Q. Sun, C. Han, Y. Guo, Q. Huang, W. A. Goddard and J. Qian, *J. Mater. Chem. A*, 2022, **10**, 16007–16015.
36 Z. Qiu, Y. Ma and T. Edvinsson, *Nano Energy*, 2019, **66**, 104118.
37 Y. Li, Y. Wu, H. Hao, M. Yuan, Z. Lv, L. Xu and B. Wei, *Appl. Catal., B*, 2022, **305**, 121033.
38 C. Hu, Y. Hu, C. Fan, L. Yang, Y. Zhang, H. Li and W. Xie, *Angew. Chem., Int. Ed.*, 2021, **60**, 19774–19778.
39 W. Q. Li, R. Y. Zhou, X. T. Wang, L. Y. Hu, X. Chen, P. C. Guan, X. G. Zhang, H. Zhang, J. C. Dong, Z. Q. Tian and J. F. Li, *J. Catal.*, 2021, **400**, 367–371.
40 J. Fester, A. Makoveev, D. Grumelli, R. Gutzler, Z. Sun, J. Rodríguez-Fernández, K. Kern and J. V. Lauritsen, *Angew. Chem.*, 2018, **130**, 12069–12073.
41 J. Zhang, J. Liu, L. Xi, Y. Yu, N. Chen, S. Sun, W. Wang, K. M. Lange and B. Zhang, *J. Am. Chem. Soc.*, 2018, **140**, 3876–3879.
42 J. Du, Y. Huang, Z. Huang, G. Wu, B. Wu, X. Han, C. Chen, X. Zheng, P. Cui, Y. Wu, J. Jiang and X. Hong, *JACS Au*, 2022, **2**, 1078–1083.
43 F. Hu, S. Zhu, S. Chen, Y. Li, L. Ma, T. Wu, Y. Zhang, C. Wang, C. Liu, X. Yang, L. Song, X. Yang and Y. Xiong, *Adv. Mater.*, 2017, **29**, 1–9.
44 X. Yu, Z. Y. Yu, X. L. Zhang, Y. R. Zheng, Y. Duan, Q. Gao, R. Wu, B. Sun, M. R. Gao, G. Wang and S. H. Yu, *J. Am. Chem. Soc.*, 2019, **141**, 7537–7543.
45 O. S. Vereshchagin, D. V. Pankin, M. B. Smirnov, N. S. Vlasenko, V. V. Shilovskikh and S. N. Britvin, *J. Alloys Compd.*, 2021, **853**, 156468.
46 Y. Zhao, M. Xi, Y. Qi, X. Sheng, P. Tian, Y. Zhu, X. Yang, C. Li and H. Jiang, *J. Energy Chem.*, 2022, **69**, 330–337.
47 S. Anantharaj, S. Kundu and S. Noda, *Nano Energy*, 2021, **80**, 105514.
48 F. Tang, T. Liu, W. Jiang and L. Gan, *J. Electroanal. Chem.*, 2020, **871**, 114282.
49 T. Harano, G. Shibata, K. Ishigami, Y. Takashashi, V. K. Verma, V. R. Singh, T. Kadono, A. Fujimori, Y. Takeda, T. Okane, Y. Saitoh, H. Yamagami, T. Koide, H. Yamada, A. Sawa, M. Kawasaki, Y. Tokura and A. Tanaka, *Appl. Phys. Lett.*, 2013, **102**, 4.
50 J. Everett, E. Céspedes, L. R. Shelford, C. Exley, J. F. Collingwood, J. Dobson, G. Van Der Laan, C. A. Jenkins, E. Arenholz and N. D. Telling, *J. R. Soc. Interface*, 2014, **11**, 20140165.
51 F. Wang, J. Jiang and B. Wang, *Catalysts*, 2019, **9**, 477.
52 P. Acharya, R. H. Manso, A. S. Hoffman, S. I. P. Bakovic, L. Kekedy-Nagy, S. R. Bare, J. Chen and L. F. Greenlee, *ACS Catal.*, 2022, **12**, 1992–2008.
53 J. Zhu, Z. Zeng and W. X. Li, *J. Phys. Chem. C*, 2021, **125**, 26229–26239.
54 F. Yu, H. Zhou, Y. Huang, J. Sun, F. Qin, J. Bao, W. A. Goddard, S. Chen and Z. Ren, *Nat. Commun.*, 2018, **9**, 1–9.
55 X. Liu, K. Ni, B. Wen, R. Guo, C. Niu, J. Meng, Q. Li, P. Wu, Y. Zhu, X. Wu and L. Mai, *ACS Energy Lett.*, 2019, **4**, 2585–2592.
56 R. A. Marquez-Montes, K. Kawashima, Y. J. Son, J. A. Weeks, H. H. Sun, H. Celio, V. H. Ramos-Sánchez and C. B. Mullins, *J. Mater. Chem. A*, 2021, **9**, 7736–7749.
57 W. Dai, X. Bai, Y. A. Zhu, Y. Zhang, T. Lu, Y. Pan and J. Wang, *J. Mater. Chem. A*, 2021, **9**, 6432–6441.
58 Z. Niu, C. Qiu, J. Jiang and L. Ai, *ACS Sustain. Chem. Eng.*, 2019, **7**, 2335–2342.
59 H. Ren, X. Sun, C. Du, J. Zhao, D. Liu, W. Fang, S. Kumar, R. Chua, S. Meng, P. Kidkhunthod, L. Song, S. Li, S. Madhavi and Q. Yan, *ACS Nano*, 2019, **13**, 12969–12979.
60 S. A. Chala, M. C. Tsai, B. W. Olbasa, K. Lakshmanan, W. H. Huang, W. N. Su, Y. F. Liao, J. F. Lee, H. Dai and B. J. Hwang, *ACS Nano*, 2021, **15**, 14996–15006.
61 J. Yu, T. Zhang, Y. Sun, X. Li, X. Li, B. Wu, D. Men and Y. Li, *ACS Appl. Mater. Interfaces*, 2020, **12**, 12783–12792.
62 X. Ding, Y. Xia, Q. Li, S. Dong, X. Jiao and D. Chen, *ACS Appl. Mater. Interfaces*, 2019, **11**, 7936–7945.
63 Y. N. Wang, Z. J. Yang, D. H. Yang, L. Zhao, X. R. Shi, G. Yang and B. H. Han, *ACS Appl. Mater. Interfaces*, 2021, **13**, 8832–8843.
64 F. Yang, X. Chen, Z. Li, D. Wang, L. Liu and J. Ye, *ACS Appl. Energy Mater.*, 2020, **3**, 3577–3585.
65 K. Zhu, X. Zhu and W. Yang, *Angew. Chem., Int. Ed.*, 2019, **58**, 1252–1265.
66 F. Dionigi, Z. Zeng, I. Sinev, T. Merzdorf, S. Deshpande, M. B. Lopez, S. Kunze, I. Zegkinoglou, H. Sarodnik, D. Fan, A. Bergmann, J. Drnec, J. F. de Araujo, M. Gliech, D. Teschner, J. Zhu, W. X. Li, J. Greeley, B. Roldan Cuenya and P. Strasser, *Nat. Commun.*, 2020, **11**, 1–10.
67 S. Chen, L. Ma, Z. Huang, G. Liang and C. Zhi, *Cell Rep. Phys. Sci.*, 2022, **3**, 100729.
68 J. Wang, L. Han, B. Huang, Q. Shao, H. L. Xin and X. Huang, *Nat. Commun.*, 2019, **10**, 1–11.
69 Y. Guan, W. Suo, Z. Zhang, Y. Wang, S. Sun and G. Liu, *Mol. Catal.*, 2021, **511**, 111725.
70 M. M. J. Li, Z. Zeng, F. Liao, X. Hong and S. C. E. Tsang, *J. Catal.*, 2016, **343**, 157–167.